C Journal of Carbon Research

MDPI

Article

Nitrogen-Doped Carbon Cryogels as Adsorbents: Efficient Removal of Organophosphate Pesticides from Water and Assessment of Toxicity Reduction

Tamara Lazarević-Pašti [1,*], Vladan Anićijević [2], Radovan Karkalić [2], Miloš Baljozović [3], Biljana Babić [4] and Igor A. Pašti [5]

[1] VINČA Institute of Nuclear Sciences—National Institute of the Republic of Serbia, University of Belgrade, Mike Petrovica Alasa 12-14, 11000 Belgrade, Serbia
[2] Military Academy, University of Defence in Belgrade, Generala Pavla Jurišića Šturma 33, 11000 Belgrade, Serbia; anicijevicj.v@gmail.com (V.A.); rkarkalic@yahoo.com (R.K.)
[3] Laboratory for Molecular Nanoscience, Paul Scherrer Institut, 5232 Villigen, Switzerland; milos.baljozovic@psi.ch
[4] Institute of Physics, University of Belgrade, 11080 Belgrade, Serbia; biljana.babic@ipb.bg.ac.rs
[5] Faculty of Physical Chemistry, University of Belgrade, Studentski Trg 12-16, 11158 Belgrade, Serbia; igor@ffh.bg.ac.rs
* Correspondence: tamara@vin.bg.ac.rs or lazarevictlj@yahoo.com

Abstract: Pesticides pose a significant threat to nontargeted organisms, and their pervasive use makes avoidance challenging. We employed nitrogen-doped carbon cryogels for the removal of organophosphate pesticides. The materials were synthesized and characterized using SEM, Raman spectroscopy, XPS, and BET analysis. Results revealed mesoporous cryogels with pore diameters ranging from 3 to 13 nm. Interestingly, the specific surface area did not change systematically with increasing nitrogen content. All investigated materials have similar composition and structural disorder. Dimethoate, malathion, and chlorpyrifos removal was investigated under stationary and dynamic conditions. Stationary conditions demonstrated successful removal of aliphatic dimethoate and malathion by all investigated materials. Conversely, the materials with the lowest and highest nitrogen content proved ineffective with aromatic chlorpyrifos. Under dynamic conditions, all materials effectively removed malathion and chlorpyrifos while exhibiting suboptimal performance for dimethoate adsorption. Application of nitrogen-doped carbon cryogels to tap water spiked with pesticides yielded successful results under the same conditions. Toxicity testing of treated samples revealed a consistent decrease in toxicity, indicating that contact with cryogels reduces the initial solution's toxicity. This result also confirms that material–pesticide interaction does not lead to the formation of more toxic byproducts. The demonstrated efficacy suggests the potential application of these materials in water treatment.

Keywords: carbon cryogel; pesticides; water remediation; adsorption; dimethoate; malathion; chlorpyrifos

check for updates

Citation: Lazarević-Pašti, T.; Anićijević, V.; Karkalić, R.; Baljozović, M.; Babić, B.; Pašti, I.A. Nitrogen-Doped Carbon Cryogels as Adsorbents: Efficient Removal of Organophosphate Pesticides from Water and Assessment of Toxicity Reduction. *C* **2024**, *10*, 56. https://doi.org/10.3390/c10020056

Academic Editors: Jorge Bedia, Carolina Belver and Craig E. Banks

Received: 19 April 2024
Revised: 28 May 2024
Accepted: 18 June 2024
Published: 20 June 2024

1. Introduction

Due to anthropogenic activity, many contaminants are continuously released into water [1–4]. Many of them are not efficiently removed by existing water treatment processes [5]. Among others, organophosphates are a major concern nowadays [6,7]. These compounds are widely used in modern agriculture and represent the main class of pesticides used for several decades. Unfortunately, organophosphate pesticides (OPs) pose a significant hazard to both humans and the majority of animals, primarily ascribed to their ability to inhibit the crucial enzyme acetylcholinesterase (AChE) [8,9]. This enzyme plays a pivotal role in terminating impulse transmission by swiftly hydrolyzing the neurotransmitter acetylcholine [10]. Accordingly, the inhibition of AChE results in the accumulation of acetylcholine, leading to heightened stimulation of nicotinic and muscarinic receptors and, consequently, disruption of neurotransmission [11,12].

Great efforts have been made to develop efficient and simple methods to determine OP levels [13–20]. However, equally important for society is to have an effective technology for removing these compounds and overcoming present and future water treatment challenges [5]. There are several paths for OP removal from the environment. Besides the chemical [21] and microbial degradation of OPs [22–24], their adsorption on different types of materials is currently an essential strategy for OP remediation. A multitude of studies can be found within the existing body of literature reporting pesticide adsorption on various materials, like mesoporous monetite [25], porous metal−organic frameworks mineral surfaces [21,26–29], organohydrotalcite [30], activated carbon [31–35], zeolites [36–38], materials from graphene family [39–42], and others. When comparing these different classes of adsorbents, it is important to note that the evaluated adsorption performance greatly depends on the experimental conditions. In particular, higher adsorbent doses increase the percentage of removed pesticide while reducing the adsorption capacity. On the other hand, the reduction in the adsorbent dose causes a rapid increase in the adsorption capacity while the percentage (i.e., uptake) of the pesticide decreases. As explained in our previous work, it is the consequence of the dynamic equilibrium between adsorbed and free pesticides [43]. Thus, for the aforementioned adsorbent, reported OP uptakes range between several and nearly 100%, while adsorption capacities range from several mg per g to hundreds or even thousands of mg per g of adsorbent, depending on the actual experimental conditions.

The adsorption-based processes are generally determined by the adsorbent's surface chemical composition and textural properties [44,45]. Due to their very favorable properties, carbonaceous materials are especially attractive for the adsorption of both organic and inorganic solutes from the aqueous phase. Their high specific surface area, wide porosity range, and the chemical nature of the activated carbon strongly influence their adsorptive capacity [46,47]. Notably, their desired properties can be easily modified by optimizing the production process or adding various dopants.

An interesting class of carbonaceous materials currently is carbon cryogels (CC). They are especially attractive due to their developed and controllable mesoporosity [48]. Carbon cryogels are predominantly synthesized through the sol–gel polycondensation process, employing precursors such as resorcinol and formaldehyde. Subsequently, the hydrogels obtained are dried and subjected to carbonization in an inert atmosphere [49,50]. In this way, stable and inert carbon materials are obtained, which are more suitable for different applications than polymeric precursors, which can easily undergo chemical changes. Noteworthy characteristics of carbon cryogels include moderately high surface areas ranging from 500 to 1200 m^2 g^{-1} and substantial mesoporous volumes exceeding 0.89 mL g^{-1} [51,52]. These specific features make carbon cryogels well suited for various applications in adsorption [52]. Additionally, surface modifications of carbon cryogels, like the introduction of different types of dopants, can alter their properties and adjust them for desired applications [53–55]. Among possible dopants, nitrogen is frequently investigated for tuning carbon properties as it can easily incorporate into the carbon lattice and cause changes in material properties [56–58].

The utilization of carbon cryogels in adsorption processes has garnered attention, particularly for the removal of specific classes of compounds [53,55,59,60]. It includes the effective elimination of certain inert pesticides that exhibit resistance to photolysis and spontaneous biodegradation. Moreover, adsorption-based processes have several advantages over other strategies for the removal of OPs from the environment, like avoidance of the use of aggressive chemicals, UV radiation, or microorganisms [61,62].

This paper aims to demonstrate the synthesis of nitrogen-doped carbon cryogels and investigate their efficacy as adsorbents for removing organophosphate pesticides from water, with a specific focus on dimethoate, malathion, and chlorpyrifos. The comprehensive characterization and assessment of nitrogen-doped carbon cryogels as adsorbents was performed, including SEM, Raman spectroscopy, XPS, and BET analysis, to elucidate their structural properties and surface functionalities. Additionally, the investigation under both stationary and dynamic conditions provides valuable insights into the adsorption behavior of these materials, particularly their effectiveness towards different pesticide classes. Furthermore, the toxicity reduction assessment of treated samples offers a novel contribution, demonstrating the potential of nitrogen-doped carbon cryogels not only for efficient pesticide removal but also for mitigating the toxicity of contaminated water. Motivated by the significant threat posed by pesticides to nontargeted organisms and the challenges associated with their widespread use, this study addresses the pressing need for efficient pesticide remediation strategies.

2. Materials and Methods

2.1. Carbon Cryogel Synthesis

The carbon cryogel synthesis process begins with the preparation of resorcinol–formaldehyde (RF) gel by polycondensation of resorcinol (R) and formaldehyde (F) with sodium carbonate (K) as a base catalyst, according to the procedure previously proposed by Momčilović et al. [49–51]. To make the RF solution, resorcinol ($C_6H_4(OH)_2$) (99%, E. Merck, Darmstadt, Germany), formaldehyde (HCHO), 36%, stabilized in methanol (Fluka Chemie, Buchs, Switzerland), sodium carbonate (Na_2CO_3) of p.a. purity (E. Merck), and distilled water (W) were used. The proportions of resorcinol to formaldehyde (mol/mol; R/F), resorcinol to water (g/mL; R/W), and resorcinol to catalyst (mol/mol; R/K) were 0.5, 0.2, and 100, respectively. Melamine was used as a nitrogen source and added to the initial solution to reach nitrogen concentrations of 2, 4, 6, 8, and 10%. After that, the RF solution with the desired amount of melamine was poured into glass tubes with an inner diameter of 10 mm, which were closed to prevent water evaporation. The samples were left to gel for 7 days: two days at room temperature (25 °C), one day at 50 °C, and four days at 85 °C. After that, the RF gel was taken out of the test tube and washed for 24 h by submerging it in a 10 times larger volume of t-butanol to replace the water in the sample with t-butanol. The washing was repeated twice. Then, the samples were kept for 24 h in a freezer at −30 °C to freeze them before drying using the freezing process in a lyophilizer. RF gels were placed in acrylic containers and dried for 24 h at a vacuum of 0.4 mbar. The RF cryogel was then carbonized in a conventional furnace at a temperature of up to 850 °C, with a heating rate of 4 °C min^{-1}, in an inert nitrogen atmosphere. The resulting material, the carbon cryogel, was powdered and stored in closed PVC boxes. Materials were labeled as CCN2%, CCN4%, CCN6%, CCN8%, and CCN10% according to the nitrogen content during synthesis.

2.2. Carbon Cryogel Characterization

The specific surface area and pore size distribution (PSD) of carbon cryogel samples doped with different amounts of nitrogen were analyzed using Surfer (Thermo Fisher Scientific, Waltham, MA, USA). PSD was estimated by applying the Barrett–Joyner–Halenda (BJH) method to the desorption branch of isotherms [63].

Raman spectra were acquired using a DXR Raman microscope (Thermo Scientific, Waltham, MA, USA) coupled with an Olympus optical microscope and a CCD detector and excited with a diode-pumped, solid-state high-brightness laser (532 nm). With an objective magnification of 10×, the laser beam was focused on the sample. A spectrograph with 900 lines per mm grating was used to measure the scattered light. The laser power on the sample was fixed at 1 mW.

A Phenom ProX (Thermo Fisher Scientific, Waltham, MA, USA) SEM was employed for SEM analysis. No deposition of the conductive layer was performed before the analysis, and the samples were analyzed as-synthesized. For the analysis of sample morphology, an acceleration voltage of 10 keV was used, while the energy dispersive X-ray analysis (EDX) was performed using an acceleration voltage of 15 keV.

XPS analysis was carried out using the SPECS Analyzer Phoibos 150 and SPECS FOCUS 500 X-ray source with a monochromatic Al Kα (1486.7 eV, 400 W). Spectrometer work function calibration was performed using C1s, Au4f, and valence band spectra of the clean reference samples, namely HOPG and Au(111) single crystal. Spectra were acquired in normal emission using SpecsLab2 software version 2.3.25PR1.0 and with a pass energy of 10 eV, providing ~450 meV resolution. No charging was observed during data acquisition. Spectra were processed using Unifit2013 with its internal database of sensitivity factors. The fitting was performed using Gaussian/Lorentzian convolution functions for components with simultaneous optimization of the Shirley spectral background. The C1s component corresponding to the sp^2 carbon signal was fitted using an asymmetric spectral line with asymmetry factor optimized during the fitting procedure (0.13 for CCN2; 0.08 for CCN4; 0.10 for CCN6; 0.02 for CCN8; 0.11 for CCN10).

2.3. Adsorption Studies

We conducted two sets of experiments to investigate the efficiency of adsorption of investigated OPs on CC. The first set was performed in a batch system, while the second was carried out in a cryogel-modified nylon membrane filter.

2.3.1. Adsorption of OPs in the Batch System

Investigated carbon cryogels were dispersed in double-distilled water, and the desired amount of dimethoate, malathion, and chlorpyrifos (Scheme 1) stock solutions (Pestanal, Sigma Aldrich, Søborg, Denmark) was added to provide the targeted concentration of adsorbent ($10\ \text{mg mL}^{-1}$) and OP ($5 \times 10^{-4}\ \text{mol dm}^{-3}$). The adsorbent and OP mixture vessel was positioned on a shaker (Orbital Shaker-Incubator ES-20, Grant-bio, Royston, UK) and left at 25 °C overnight to ensure equilibrium. The pH was not specifically adjusted, but it was controlled and found to be around 6 (±0.2) in all the cases. When equilibration was achieved, we centrifuged the mixture for 10 min at 14,500 rpm. Next, the supernatant was filtered through the nylon filter membrane. The OP concentration was determined using UPLC analysis (described below, Section 2.4), while its physiological effects were determined by Ellman's procedure, as explained in Section 2.5. Control experiments were performed identically but without adsorbents, and no OP degradation was confirmed within the timeframes of the described experiments. The performance of each adsorbent was quantified as the OP uptake (the percentage of adsorbed OP from the solution), defined as OP uptake (%) = $100 \times (C_0 - C)/C_0$, where C_0 and C stand for the OP concentration before and after the adsorption experiment, respectively [32].

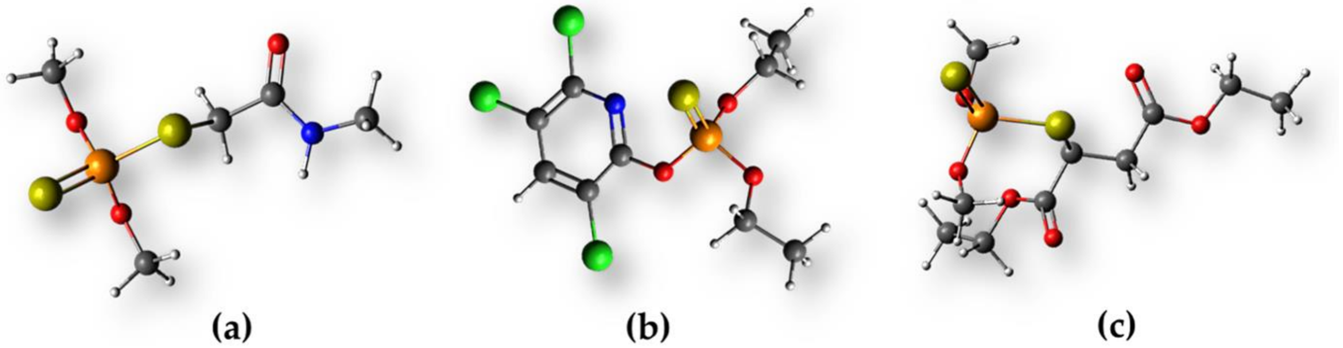

Scheme 1. The structures of (**a**) dimethoate, (**b**) chlorpyrifos, and (**c**) malathion. Black—carbon, red—oxygen, blue—nitrogen, yellow—sulphur, green—chlorine, white—hydrogen.

2.3.2. Adsorption of OPs via Cryogel-Modified Nylon Membrane Filter

To investigate the possibility of using the studied carbon cryogels as adsorbents in filters, we modified a commercial nylon membrane filter to include the layer of active material (Scheme 2). The modification was conducted as follows. The total amount of 10 mg of each sample was dispersed in deionized water and injected into the commercial nylon filter (KX Syringe Filter, Kinesis, Cole Parmer, St. Neots, UK, pore size 220 nm).

Excess water was removed from the modified filter by compressed air. After that, 1 mL of 5×10^{-4} mol dm^{-3} OPs was injected through the modified filter. The flow rate was 1 mL min^{-1}. In these experiments, the OP to adsorbent mass ratio was kept the same as in the batch adsorption experiments to have a direct comparison. The filtrate was subjected to the UPLC analysis to determine the concentration of OPs (described below, Section 2.4). Also, the physiological effects of filtrates were determined as described below (Section 2.5). Control experiments were performed using the nonmodified filters. Upon comparing the concentrations of OP before and after filtration through the unmodified filter, we validated that the observed removal of OP from the filtrate, as witnessed in experiments involving modified filters, is not attributable to the nylon membrane. The efficiency of a modified filter towards OP removal was also quantified as the OP Uptake (see Section 2.3.1). After the experiments, modified filters were disassembled to check for the uniformity of the adsorbent layer. In each case, we observed a uniform distribution of the adsorbent over the nylon membrane. Moreover, the integrities of nylon membranes were not compromised during the experiments.

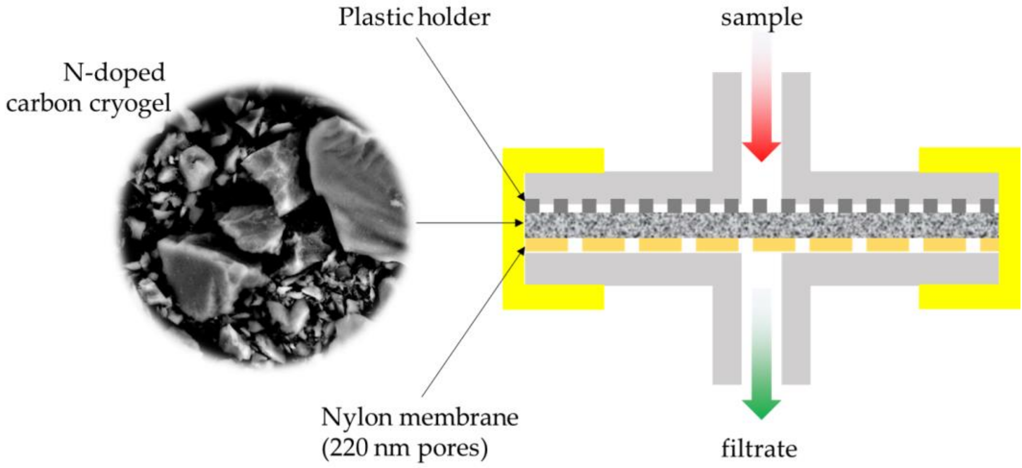

Scheme 2. The scheme of a modified nylon filter used in this study.

2.4. UPLC Analysis

The Waters ACQUITY Ultra Performance Liquid Chromatography (UPLC) system, coupled with a tunable UV detector controlled by the Empower 3 version software, was employed for the study. Chromatographic separations were conducted using an ACQUITY UPLC™ BEH C18 column with dimensions of 1.7 µm, 100 mm × 2.1 mm (Waters). For the analysis of dimethoate, malathion, and chlorpyrifos solutions, isocratic conditions were applied with specific mobile phase compositions: 10% acetonitrile and 90% water (*v*/*v*) for dimethoate; 60% acetonitrile and 40% water (*v*/*v*) for malathion; and 80% acetonitrile and 20% water (*v*/*v*) for chlorpyrifos. The eluent flow rate was set at 0.2 mL min^{-1}, and the injection volume was maintained at 10 µL. Optical detection of dimethoate was performed at 200 nm, malathion at 230 nm, and 225 nm was used for chlorpyrifos. Under the described conditions, dimethoate, malathion, and chlorpyrifos retention times were 1.73 ± 0.05, 2.38 ± 0.05, and 2.57 ± 0.05 min, respectively.

2.5. Toxicity Assessment

Toxicity assessment of the samples before and after adsorption experiments was carried out via measurements of AChE inhibition. Besides performing AChE inhibition measurements to quantify the toxicity of the investigated OPs, these tests also provide information about potential transformations of OPs into more toxic forms due to the contact with adsorbents. It particularly relates to the formation of oxo-forms of OPs, which are much more toxic than corresponding thio-forms [39]. These oxidation products can exert toxic effects at concentrations below the detection limits of UPLC. Hence, it is important to estimate the toxicity of the final samples via bioanalytical assay since their limit of detection is lower. AChE activity was assayed according to the modified Ellman's procedure. [64] This procedure is described in detail in [39], and we provide it here for the sake of completeness. The in vitro experiments were performed by exposure of 2.5 IU commercially purified AChE from electric eel to OP solutions obtained before and after the adsorption experiments at 37 °C in 50 mM PB pH 8.0 (final volume 0.650 mL). The enzymatic reaction was started by the addition of acetylcholine-iodide (AChI) in combination with 5,5′-dithiobis(2-nitrobenzoic acid) (DTNB) as a chromogenic reagent and continued for 8 min until stopped by 10% sodium dodecyl sulfate (SDS). The enzymatic reaction product, thiocholine, reacts with DTNB and forms 5-thio-2-nitrobenzoate, whose optical adsorption was measured at 412 nm. It should be noted that in these measurements, the enzyme concentration was chosen to give an optimal spectrophotometric signal. Physiological effects were quantified as AChE inhibition given as AChE inhibition = $100 \times (A_0 - A)/A_0$, where A_0 is the AChE activity in the absence of OP and A is the AChE activity measured after exposure to a given OP.

3. Results

3.1. Carbon Cryogel Characterization

3.1.1. Scanning Electron Microscopy

The morphology of the investigated CC samples was studied using scanning electron microscopy, and the micrographs are shown in Figure 1. From the results shown, it can be concluded that doping cryogels with different amounts of nitrogen did not lead to significant differences in the surface morphology of the samples. The particle sizes are approximately the same, while there are indications of long fiber-like structures building the particles and forming the pore network.

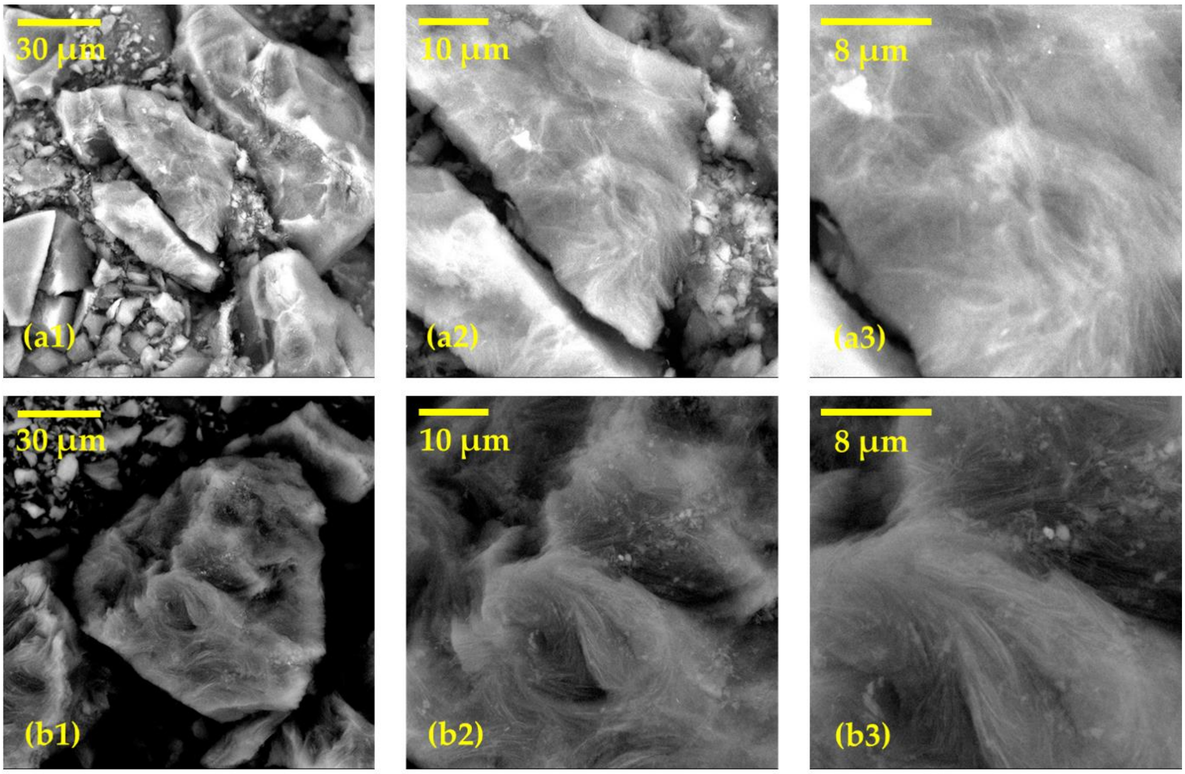

Figure 1. SEM images of CCN2 (**a**) and CCN10 (**b**) at three different magnifications ((**a1**,**b1**)—2000× magnification; (**a2**,**b2**)—5000× magnification, (**a3**,**b3**)—10,000× magnification).

3.1.2. BET Analysis

The specific surface area and pore size distribution of nitrogen-doped carbon cryogels were obtained by BET analysis. These results are shown in Figure 2 and Table 1.

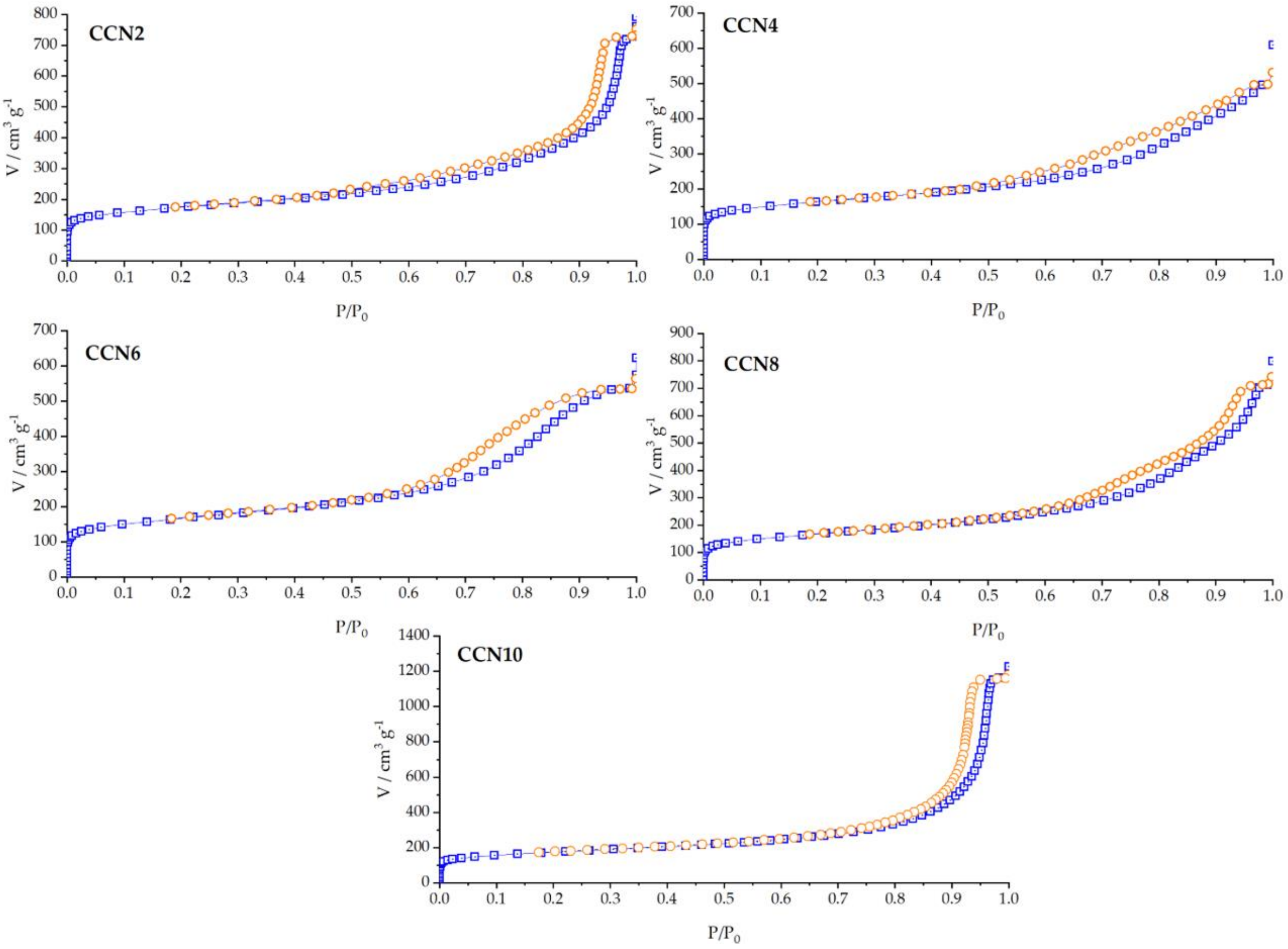

Figure 2. Adsorption and desorption isotherm of nitrogen adsorbed on carbon cryogels doped with nitrogen. The results are presented as the fraction of adsorbed and desorbed nitrogen on the material as a function of the relative pressure at −196 °C (squares—adsorption, circles—desorption).

Table 1. Porous properties of investigated carbon cryogels.

Sample	Specific Surface Area (BET Method) /m^2 g^{-1}	Average Pore Radius (APR)/nm	Cumulative Volume /cm^3 g^{-1}
CCN2%	628	8.5	1.2
CCN4%	586	3.5	0.8
CCN6%	589	3.6	0.9
CCN8%	595	5.4	1.2
CCN10%	621	12.3	1.9

From the results shown in Figure 2, it can be seen that all isotherms are of type IV according to the IUPAC classification [65] and have a hysteresis loop, which is typical for mesoporous materials [66]. The hysteresis loop of the CCN2% material is of the H3 type, typical for aggregates of weakly interacting plate structures and the existence of a wider distribution of pores. The hysteresis loop of the CCN4% material is of type H4, which indicates narrow pores in the form of cracks. On the other hand, for the CCN8% material, type H2b hysteresis is observed, indicating poorly defined uniform mesopores that are partially blocked. Materials CCN6% and CCN10% are characterized by a hysteresis loop of type H1, which is characteristic of pore systems in the form of narrow channels. This form of hysteresis is always associated with a narrow pore size distribution. A large volume adsorbed at low relative pressure indicates the presence of micropores in all tested samples.

Based on the presented results and using the BET method, the specific surface areas of the materials, S_{BET}, were determined and shown in Table 1. It can be noted that the specific surface areas of all materials are in the range between 586 and 628 m^2 g^{-1}, and that the specific surface area does not change systematically with increasing nitrogen content. In fact, all materials have a similar surface. The difference is about 5% due to the large approximations in the surface calculation model [63,67]. Also, the calculated surfaces are in accordance with the literature and data for similar materials [49,68,69].

The pore size distribution (PSD) of the studied materials is given in Figure 3. From the results shown, we see that the pore diameters of the investigated cryogels have values between 3 and 13 nm, which means that the materials are mesoporous according to the IUPAC classification [70]. Also, the pore radius does not change systematically with an increase in the amount of doped nitrogen, as shown in Table 1. On the distribution diagrams of the pore radius for samples with 2, 4, 6, and 10% doped nitrogen, one peak can be observed, which means that the materials are homogeneous. For the material with 8% doped nitrogen, two peaks are observed, indicating the dominance of pores with two different radii. We note that the obvious lack of a monotonous trend connecting the nitrogen content and the average pore radius (Table 1) is not surprising. Here, we observed a minimum of the average pore radius along the series for CCN6%, while some previous works reported no apparent connection between the nitrogen content and the pore size [71–73]. Revealing such connections would certainly be useful for precise materials engineering, but analyzing the mechanism of pore formation in nitrogen-doped carbons is beyond the scope of the present work.

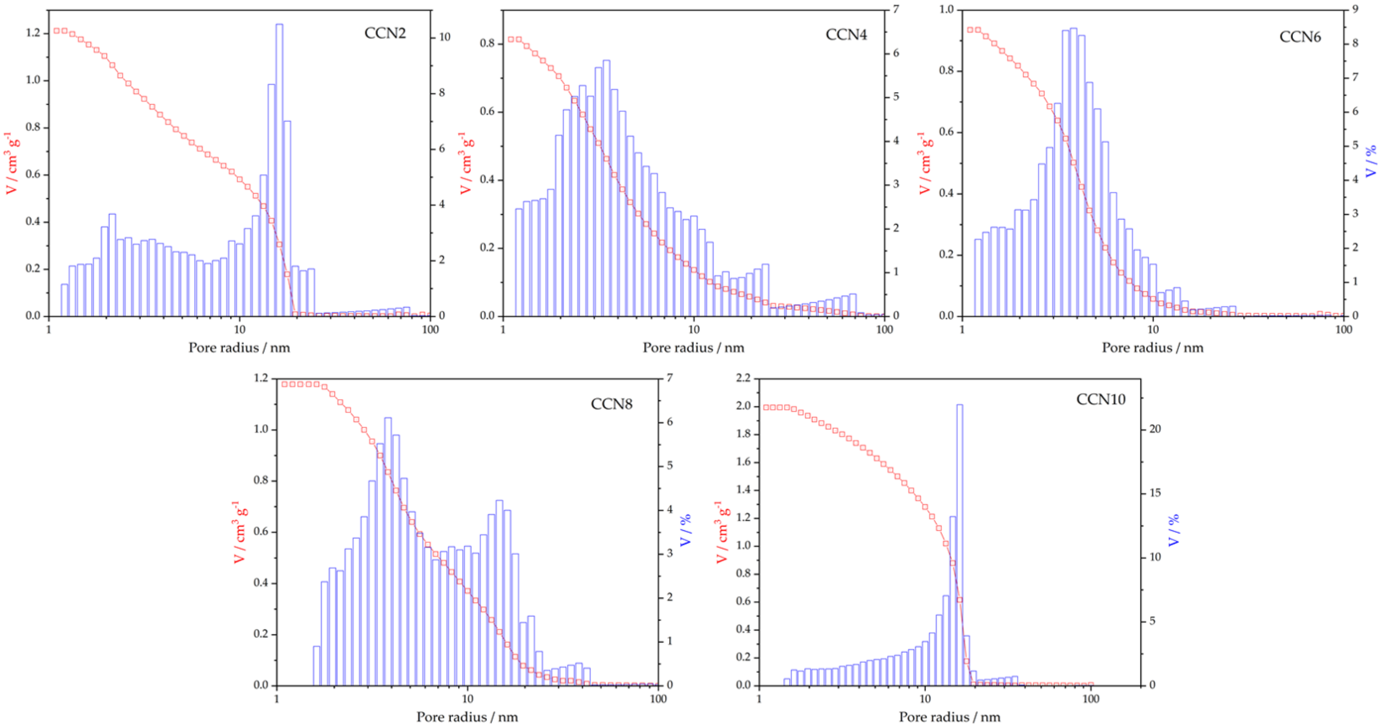

Figure 3. Pore size distribution for investigated carbon cryogels.

3.1.3. Raman Analysis

Figure 4 shows the Raman spectra of the investigated materials. Two broad peaks are observed in all spectra: D peak at about 1350 cm^{-1} and G peak at about 1600 cm^{-1}. These peaks are characteristic of disordered materials. The D band represents the defect region and originates from the out-of-plane vibrations attributed to the presence of structural defects, while the G band represents the graphitic region and is the result of in-plane vibrations of the sp^2-bonded carbon atoms. Information about the disorder in the material can be obtained from the intensity ratio of the D and G bands. The closer their ratio is to 1, the more ordered the material is. Conversely, values significantly greater than 1 indicate a high disorder in the materials.

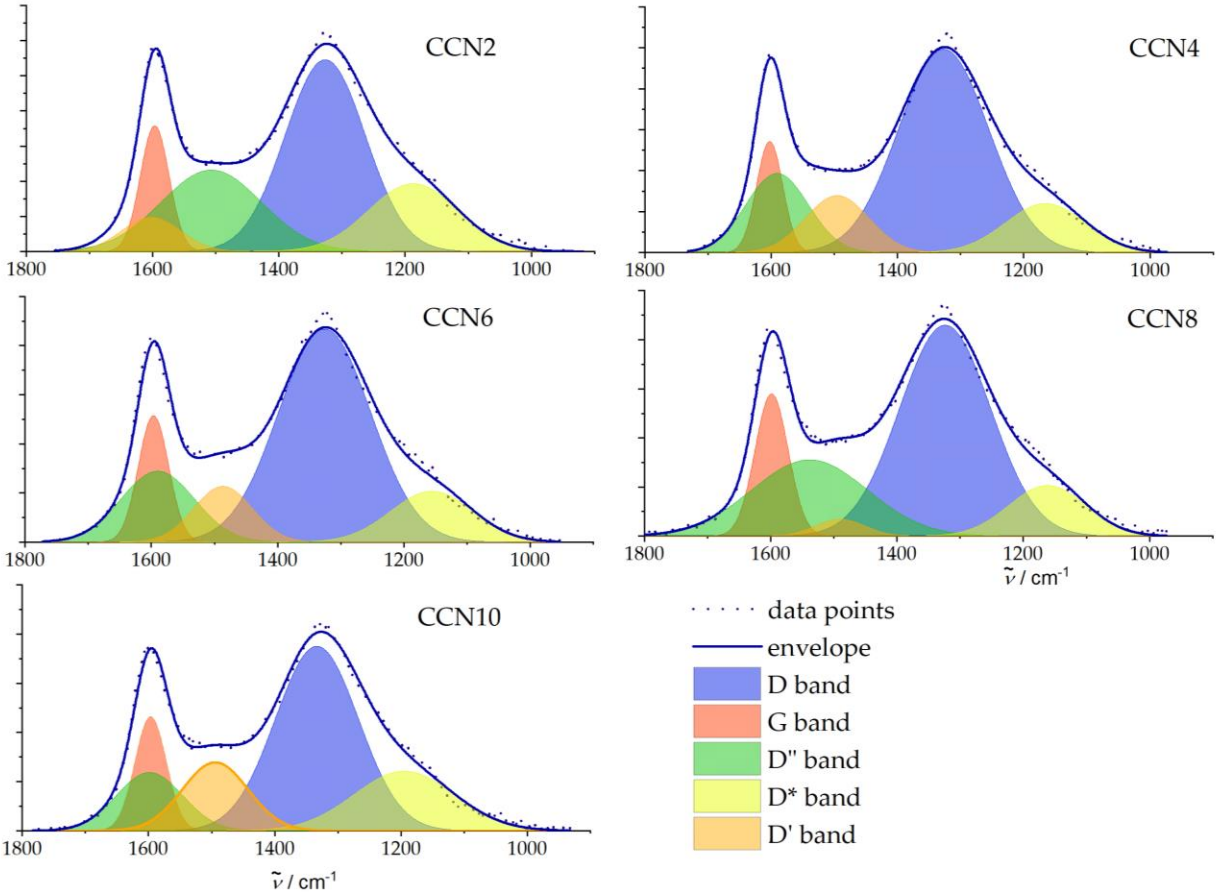

Figure 4. Raman spectra of carbon cryogels doped with nitrogen.

The parameters of the Raman spectra for the investigated materials are given in Table 2. Since the I_D/I_G ratio is greater than 1 in all cryogels, this means that their structure is disordered [74,75]. As for other properties, there is no systematic change in the I_D/I_G ratio with the concentration of the N dopant, suggesting that the incorporation of N in the carbon structure at the concentrations used in this work all induce similar structural changes. Such a situation was observed in the literature before, suggesting that there is no clear connection between the nitrogen content in nitrogen-doped carbon and the I_D/I_G ratio, or at least the monotonous connection between the nitrogen content and the I_D/I_G ratio [71,72,76], while additional difficulties in the analysis of Raman spectra could be induced by hysteresis during ordering at higher temperatures [77]. Such hysteresis likely appeared as the G band is located at high wavenumbers while the I_D/I_G ratio is above 1.5 for all the samples. This would position our samples somewhere in the transition range between stage 1 and stage 2 of the amorphization trajectory [77], but the XPS results suggest that sp^3 carbon is present (see Section 3.1.4, the content of the sp^3 carbon places our samples between stage 2 and stage 3 of the amorphization trajectory), confirming the appearance of hysteresis during the carbonization of the precursor and nonmonotonous variations in the I_D/I_G ratio along the series. As in the case of the pore network formation, we do not describe the mechanism of the defect formation in our samples and proceed with the analysis of the surface chemical composition.

Table 2. Porous properties of the investigated carbon cryogels.

	D* (D4)	D (D1)	D″ (D3)	G	D′ (D2)	I_D/I_G
Sample	**Wavenumber/cm^{-1}**					
CCN2%	1187	1327	1602	1597	1507	1.52
CCN4%	1166	1327	1495	1602	1591	1.79
CCN6%	1162	1324	1490	1599	1539	1.48
CCN8%	1156	1326	1487	1597	1590	1.68
CCN10%	1195	1333	1494	1597	1599	1.62

3.1.4. XPS Analysis

The X-ray photoelectron spectra of the examined materials were recorded to determine their structure and chemical composition. The spectra of C1s, O1s, and N1s levels are shown in Figure 5. The chemical composition of the tested materials is shown in Table 3. Survey spectra for all the samples are provided in the Supplementary Materials (Figure S1), while the high-resolution spectra for the samples excluding CCN10 are given in Figure S2.

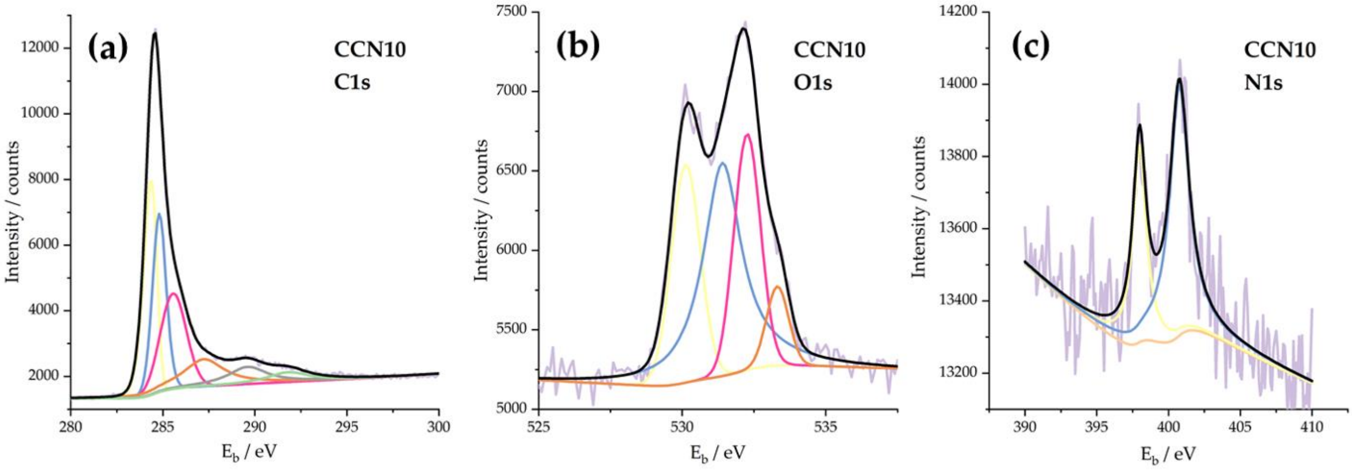

Figure 5. C1s (**a**), O1s (**b**), and N1s (**c**) X-ray photoelectron spectra of the CCN10 sample.

Table 3. Surface chemical composition of the investigated carbon cryogels based on XPS survey spectra.

Sample	C at.%	N at.%	O at.%
CCN2%	97.06	0.24	2.70
CCN4%	98.19	0.39	1.42
CCN6%	97.55	0.59	1.85
CCN8%	96.74	0.73	2.53
CCN10%	93.90	1.00	5.08

From Table 3, it is evident that the amount of nitrogen incorporated into the material during the synthesis is about 10% of the added amount. By analyzing the displayed spectra, the content of carbon, oxygen, and nitrogen can be obtained, and the existence of functional groups containing these elements can be detected. All tested cryogels have bands with the same maximum position, but their intensities differ, as shown in Table 4. Band intensities are directly proportional to the content of certain groups in the material, and these data can be used for quantitative composition determination. The binding energy positions slightly vary from sample to sample (±0.2 eV), and the positions summarized in Table 4 are the averaged ones.

Table 4. The relative contributions of various surface chemical groups in the studied cryogels, as determined using XPS analysis.

Element	E_b/eV (±0.2 eV)	Assignation	Relative Contribution of Each Functional Group/% CCN2%	CCN4%	CCN6%	CCN8%	CCN10%
C	284.5	C=C (sp^2)	27.6	32.7	56.3	27.4	26.8
	285.1	C–C (sp^3)	20.5	24.6	14.7	24.8	23.3
	285.9	C–O$_x$	20.3	15.5	14.3	19.3	23.1
	287.5	C=O, N−C=O	15.9	9.2	8.1	12.5	13.8
	290.0	$\pi\rightarrow\pi^*$	9.7	8.5	-	10.3	8.1
	292.5	$\pi\rightarrow\pi^*$ (N-containing C)	5.7	9.2	5.6	4.7	4.7
O	530.3	C=O	15.2	35.3	29.2	5.1	24.8
	531.8	C–O	50.6	25.1	40.9	63.4	43.4
	532.5	C–O–C	34.1	37.4	30.0	31.5	24.6
	533.7	C–OH, H–OH	-	-	-	-	6.9
N	398.8	Pyrrolic/Pyridonic N	50.1	28.1	34.3	38.5	35.2
	400.8	Quaternary N	49.9	71.9	65.7	61.5	64.8

In the case of C1s spectra (Figure 5), deconvolution was performed for all the examined materials. Bands with different intensity maximum positions depending on the binding energy were obtained and can be assigned to different groups. The band with the highest intensity, which has a maximum at 284.5 eV, can be attributed to the C=C sp^2 bond, while other bands are also present: C–C at 285.1 eV, which is attributed to the sp^3 bond; C–O$_x$ at 285.9 eV attributed to the epoxy and hydroxyl groups [78]; C=O and N−C=O band at 287.5 eV [79]; and finally a weak intensity band at 290.0 eV attributed to $\pi\rightarrow\pi^*$ [80]. The component at 292.5 eV is ascribed to the same transition in N-containing carbons [81] and carbons rich in carboxylic groups [82,83].

O1s spectra (Figure 5) have a broad band in the region from about 530 to about 535 eV, which was deconvolved into several components based on references [78,84,85]. This band originates from various types of oxygen moieties. Bands with maxima at 530.3 and 531.8 eV are attributed to the C=O and C–O moieties [86], at 532.5 eV are attributed to the C–O–C bond, and at 533.7 eV belonging to C–OH and H–OH sp^3 bonds [87]. N1s spectra (Figure 5) show the presence of two main types of nitrogen moieties in the carbon structure: pyrrolic/pyridonic and quaternary nitrogen [88].

3.2. OP Removal via Adsorption on Carbon Cryogels

3.2.1. Adsorption of OPs in the Batch System

The adsorption of 5×10^{-4} mol dm^{-3} malathion, chlorpyrifos, and dimethoate on 10 mg mL^{-1} carbon cryogels dopped with nitrogen was investigated. The incubation time of pesticides and adsorbents was 24 h, so the concentrations determined in the supernatant are considered to be equilibrium concentrations. The results are presented in Figure 6.

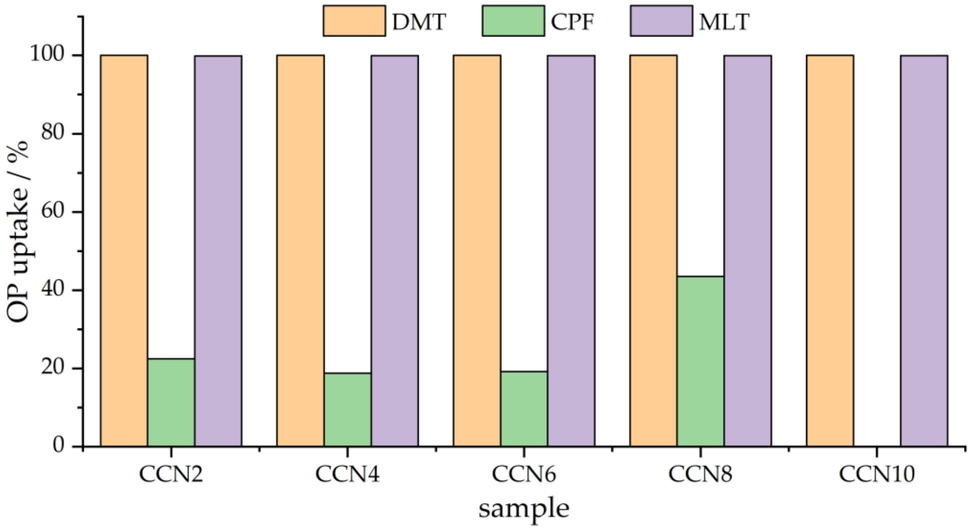

Figure 6. OPs removal using N-doped carbon cryogels under batch conditions.

From the data presented in Figure 6, it can be seen that aliphatic organophosphates, dimethoate, and malathion are very successfully adsorbed on all tested cryogels under static conditions in batch studies. Dimethoate could not be detected in the supernatant decanted after adsorption. This means that the dimethoate concentration dropped below 1×10^{-8} M, which is the detection limit of the instrument used for this analysis (UPLC) under the given experimental conditions. These results suggested that all dimethoate from the solution is adsorbed on all tested materials. In the case of malathion, it was possible to detect low concentrations of pesticides in the decanted supernatants, in concentrations ranging from 10^{-7} to 10^{-8} mol dm^{-3}, which is practically negligible considering that the initial malathion concentration was 5×10^{-4} mol dm^{-3}.

On the other hand, with aromatic chlorpyrifos, the situation is different. The material with the highest nitrogen content, CCN10, turned out to be completely inefficient in this case. In contrast, the CCN8 proved to be the most suitable adsorbent, which adsorbed 43% of the available chlorpyrifos. Materials CCN2, CCN4, and CCN6 adsorbed about 20% of the available pesticide. To understand such a trend, it is necessary to consider two different contributions—surface chemical composition and pore sizes. First, with the increase in nitrogen content, the polarity of the surface is expected to increase due to the charge redistribution caused by the differences in electronegativities of carbon and nitrogen. On the other hand, there is a change in the pore sizes with nitrogen content increase, and the sample CCN8 has pores above 4 nm, being optimal for chlorpyrifos removal [31], in addition to lower surface oxygen content compared to CCN2 and CCN10 samples, enabling the interactions of aromatic moiety of chlorpyrifos with the surface. Thus, the maximum adsorption of chlorpyrifos by CCN8 is due to sufficiently large and optimal pore sizes, able to accommodate higher amounts of chlorpyrifos compared to samples with larger and smaller pores, and relatively lower surface oxygen content compared to the samples with larger pores and larger pore volumes (CCN2 and CCN10).

3.2.2. Adsorption of OPs in the Filter System

The adsorption of 5×10^{-4} mol dm^{-3} malathion, chlorpyrifos, and dimethoate on 10 mg mL^{-1} carbon cryogels dopped with nitrogen was also examined under the dynamic conditions described in Section 2.3.2 in filter studies. For each of the tested adsorbents, 10 mg was injected into nylon filters. Next, 1 mL of 5×10^{-4} mol dm^{-3} solution of each tested organophosphate was filtered through the modified nylon filter within 1 min. In the filtrate, the concentration of the remaining pesticides was determined chromatographically. The results are presented in Figure 7.

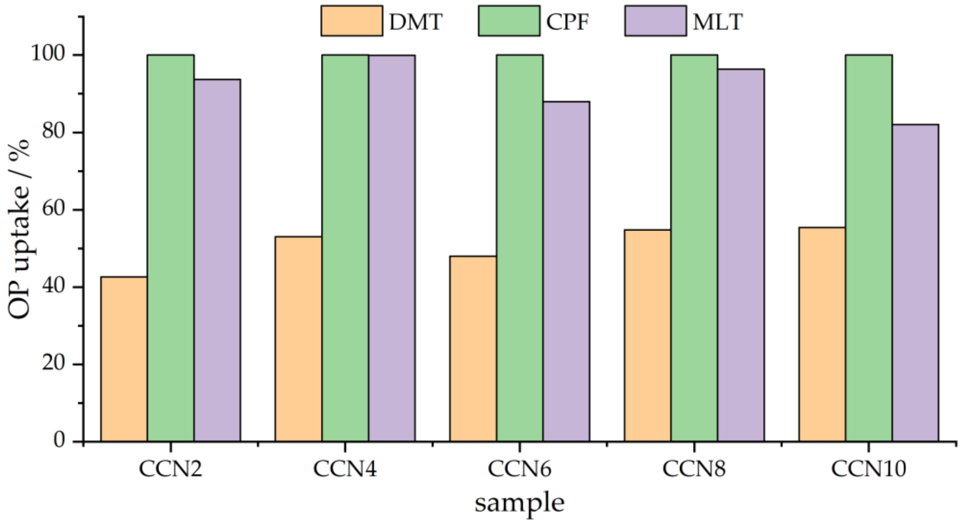

Figure 7. OPs removal using the filter system with N-doped carbon cryogels.

Adsorption using filters under dynamic conditions showed a different trend of results compared to the experiment in batch. From the results given in Figure 7, it can be seen that aromatic chlorpyrifos is the one that is completely adsorbed to all the tested materials. The remaining traces of pesticides in the filtrates could not be detected since their concentration was below the instrument's detection limit (1×10^{-8} mol dm^{-3}). It is also obvious that under dynamic conditions, aliphatic malathion is adsorbed in a high percentage on all investigated cryogels. Material CCN4 showed the best result and almost completely adsorbed the initial amount of pesticides (99%). Material CCN8 adsorbed 96% malathion and material CCN4 94% under the given experimental conditions. CCN6 and CCN10, with 88% and 82% of adsorbed malathion, respectively, showed slightly lower performance. Even though the percentage of adsorbed pesticides varied from 82 to 99, we can say that all the investigated materials under dynamic conditions are effective adsorbents for the remediation of malathion due to the fact that amounts that could be found in real samples are significantly lower than those that were investigated [89].

Unlike chlorpyrifos and malathion, the investigated materials yielded significantly inferior results in terms of dimethoate adsorption under dynamic conditions. The adsorption percentages range from 43% to 56% of the initial concentration. The uptake increased with the increase in nitrogen content in the adsorbent structure. It is evident that nitrogen addition has a favorable effect on dimethoate adsorption efficiency under dynamic conditions, but nitrogen content does not play a significant role in the given framework. Although the adsorption efficiency under these conditions is about 50%, this result, although significantly poorer than the adsorption of the other two pesticides, is by no means negligible, considering the already discussed situation in the environment [89]. Moreover, there are cases when the adsorption rate is critical (e.g., adsorption of chemical warfare with the structure of organophosphate) and plays a more significant role than adsorption efficiency. Under those circumstances, materials that adsorb many potential pollutants under dynamic conditions have the advantage, even if adsorption efficiency is not 100%.

3.2.3. Physiological Effects

As explained in Section 2.5, we analyzed the physiological effects of purified water samples, considering the ones obtained in batch and filtration experiments. As shown in Table 5, AChE inhibition is induced for the initial concentration of OPs used in the adsorption experiments, which is connected to the neurotoxic effects of OPs. Also, it is noticeable that AChE inhibition for the samples without the adsorbent for batch studies decreases in comparison to those in filter studies. This discrepancy is attributed to the previously discussed instability of OPs at room temperature, where batch samples are exposed for 24 h, whereas filter studies involve only a brief exposure of a few minutes. Chlorpyrifos showed complete inhibition of AChE activity under the given experimental conditions for both initial and apparent initial concentrations since it is highly toxic in both amounts.

Table 5. Inhibition of AChE activity in the presence of chlorpyrifos, malathion, and dimethoate before (without adsorbent added) and after the adsorption on the investigated carbon cryogels in batch and filter.

	AChE Inhibition (% of Control)					
		Batch			**Filter**	
Sample	**Chlorpyrifos**	**Malathion**	**Dimethoate**	**Chlorpyrifos**	**Malathion**	**Dimethoate**
No adsorbate	100 ± 1	72 ± 2	13 ± 1	100 ± 1	85 ± 3	17 ± 1
CCN2%	25 ± 1	0	0	0	13 ± 1	0
CCN4%	38 ± 3	0	0	0	0	0
CCN6%	32 ± 2	0	0	0	26 ± 2	0
CCN8%	0	0	0	0	8	0
CCN10%	88 ± 2	0	0	0	39 ± 2	0

However, after the adsorption of OPs on carbon cryogels, purified water samples in the cases of malathion and dimethoate in batch studies and chlorpyrifos and dimethoate in filter studies induced no AChE inhibition. Other samples induced lower AChE inhibition compared to nonpurified samples, suggesting a decrease in solution toxicity after incubation with all investigated carbon cryogels. This observation also confirms the absence of oxidation and the formation of more toxic byproducts during the interaction between OPs and cryogels.

3.2.4. Real Samples

Carbon cryogels doped with nitrogen were successfully applied to real tap water samples spiked with tested OPs under the same conditions as described in previous sections. The results are shown in Figure 8. It can be seen that the influence of the matrix is not significant in both static and dynamic conditions. The investigated materials were successfully used for real tap water sample purification.

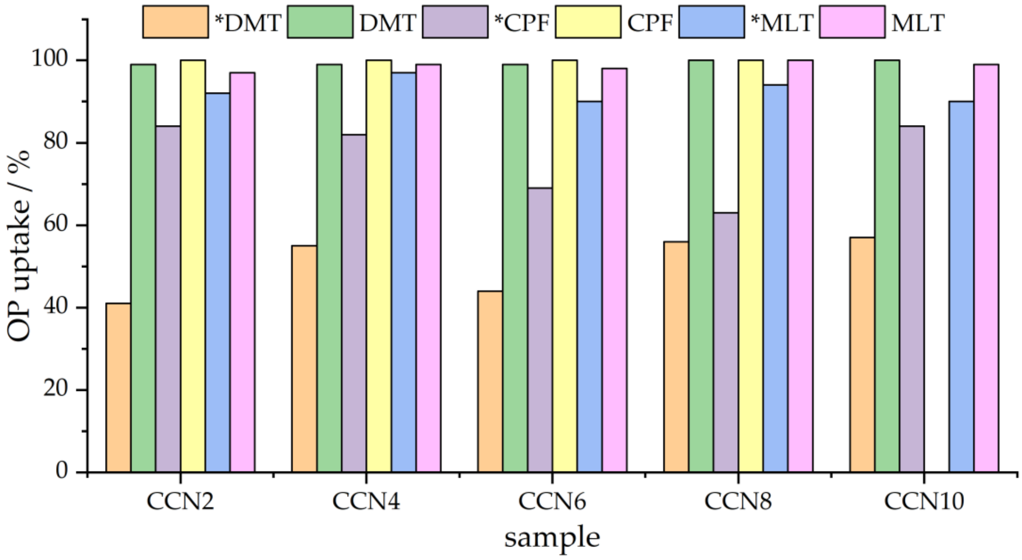

Figure 8. OPs uptake from spiked tap water samples under stationary and dynamic conditions (marked by *).

4. Discussion

4.1. Linking Adsorption Performance to the Properties of the Materials

Based on the obtained results concerning materials characterization, it is evident that the addition of nitrogen and its incorporation in the cryogel structure does not lead to variations in carbon morphology. However, it changes the chemical composition slightly and induces changes in the textural properties. The CCN2 and CCN10 samples have the highest specific surfaces and the widest pores, while the samples in the middle of the series have somewhat smaller specific surfaces and significantly narrower pores.

Under stationary conditions, both MLT and DMT are adsorbed to a high degree, while CPF is adsorbed much less. This finding is discussed in more detail in the next section. However, considering the high uptake of DMT and MLT, it is likely that under stationary conditions, differences in the pore structure are diminished by sufficient time given to OPs to enter the pores. The adsorption is likely to take place via physisorption through a number of surface functional groups observed by XPS (Table 4), which bear partial charges and interact in this way with MLT and DMT. CPF has an aromatic structure, so it is likely that interactions with CCN samples take place via π-π stacking interactions. The highest concentration of sp^2 moieties is observed in the case of the CCN6 samples (Table 4, 56.3% of total observed surface carbon moieties). However, this sample also has an average pore diameter under 4 nm, which could lead to hindered adsorption of CPF on the pore walls [31]. Thus, we believe that in the case of the CCN series of samples, the adsorption performance is determined by a complex interplay between the surface chemistry and texture of the adsorbents.

4.2. Comparison of Adsorption Efficiency in Batch and Filter Studies

To compare the adsorption of dimethoate, chlorpyrifos, and malathion on carbon cryogels doped with different amounts of nitrogen in batch and filter studies, we expressed adsorption efficiency as mg of adsorbed OP/g of adsorbent. The results are given in Table 6.

Table 6. Adsorption efficiency (adsorption capacity, mg of adsorbed OP/g of adsorbent) for adsorption of dimethoate, chlorpyrifos, and malathion on carbon cryogels doped with nitrogen in batch and filter.

	Adsorption Capacity, mg of Adsorbed OP per g of Adsorbent					
	Batch			Filter		
Sample	**Chlorpyrifos**	**Malathion**	**Dimethoate**	**Chlorpyrifos**	**Malathion**	**Dimethoate**
CCN2%	7.6	4.6	2.2	4.9	15.5	17.5
CCN4%	7.6	4.6	1.8	6.1	16.5	17.5
CCN6%	7.6	4.6	1.9	5.5	14.5	17.5
CCN8%	7.6	4.6	4.2	6.3	15.9	17.5
CCN10%	7.6	4.6	0.0	6.4	13.5	17.5

It is expected that the adsorption efficiency for all studied OP will be higher in batch than in filter studies. However, the results presented in Table 6 reveal a contrasting trend, indicating that the efficiency of chlorpyrifos adsorption on the studied adsorbents is higher in filter studies compared to batch studies. This can be explained by the fact that chlorpyrifos is not stable under given experimental conditions (24 h of incubation with adsorbent at room temperature 25 °C). Due to that, chlorpyrifos is partially hydrolyzed to 3,5,6-trichloro-2-pyridinol (TCP) and diethyl phosphorothioate [90], and its apparent initial concentration is lower under the batch condition. Consequently, it appears like the experiments in the filter were performed with higher initial concentration, so the adsorption efficiency obtained is also higher. Moreover, TCP and diethyl phosphorothioate have structures analog to the parts of the structure of chlorpyrifos, but they are smaller dimensions. The significance of this lies in the enhanced ability of TCP and diethyl phosphorothioate to interact with the adsorbent's pores and rapidly occupy adsorption sites on its surface. This phenomenon may introduce additional steric hindrance for aromatic chlorpyrifos, blocking the pores and contributing to higher efficiency in filter studies than batch studies.

In the case of malathion, it can be observed that the adsorption efficiency is also higher in the filter studies, as in the case of chlorpyrifos (Table 6). Malathion's instability can also elucidate this type of behavior at room temperature. However, in this case, it is evident that all nondegraded malathion is adsorbed on all the investigated cryogels, and there is no competition with its degradation products. This difference can be explained by its aliphatic structure compared to aromatic chlorpyrifos.

Aliphatic dimethoate showed the expected results: adsorption efficiency was higher in batch studies compared to the filter studies. It is in accordance with dimethoate stability, which is the highest of all studied organophosphates [91].

5. Conclusions

In conclusion, our study elucidates the complex relationship between the properties of nitrogen-doped carbon cryogels and their adsorption performance towards organophosphate pesticides. Despite minimal alterations in carbon morphology, nitrogen incorporation induces significant changes in textural properties and subtle variations in chemical composition, shaping adsorption behavior. Under stationary conditions, the notable uptake of aliphatic dimethoate and malathion suggests efficient physisorption facilitated by surface functional groups, while the lower adsorption of aromatic chlorpyrifos suggests alternative mechanisms, possibly involving π-π stacking interactions. Comparing batch and filter studies, an interesting trend emerges, where contrary to conventional expectations, higher efficiency is observed in filter studies for chlorpyrifos and malathion due to their instability under experimental conditions, leading to hydrolysis into smaller, more readily adsorbable compounds. On the other hand, the persistence of dimethoate results in higher efficiency in batch studies. Overall, our findings highlight the complexity of OP adsorption onto nitrogen-doped carbon cryogels, emphasizing the need for a comprehensive understanding of material properties and OP characteristics for effective pesticide remediation strategies. By shedding light on the complicated interplay between chemical structure, surface properties, and adsorption mechanisms, our study contributes to the advancement of adsorbent materials for environmental applications, making way for innovative and sustainable water treatment technologies.

Supplementary Materials: The following supporting information can be downloaded at: https://www.mdpi.com/article/10.3390/c10020056/s1, Figure S1: XPS survey spectra of the studied samples; Figure S2: C1s, O1s, and N1s X-ray photoelectron spectra of the CCN samples.

Author Contributions: Conceptualization, T.L.-P. and I.A.P.; methodology, T.L.-P., I.A.P., M.B. and B.B.; validation, V.A., B.B. and R.K.; formal analysis, T.L.-P., V.A., I.A.P., B.B. and M.B.; investigation, all authors; data curation, V.A., R.K. and M.B.; writing—original draft preparation, T.L.-P. and I.A.P.; writing—review and editing, all authors; visualization, T.L.-P. and I.A.P.; supervision, T.L.-P. and I.A.P.; funding acquisition, T.L.-P. and I.A.P. All authors have read and agreed to the published version of the manuscript.

Funding: This research was funded by the Serbian Ministry of Education, Science, and Technological Development, grant numbers 451-03-66/2024-03/200017 and 451-03-65/2024-03/200146.

Data Availability Statement: Data used in this work are available upon a reasonable request to the corresponding authors.

Acknowledgments: The authors would like to thank Danica Bajuk-Bogdanović for recording Raman spectra.

Conflicts of Interest: The authors declare no conflicts of interest.

References

1. Mishra, R.K.; Mentha, S.S.; Misra, Y.; Dwivedi, N. Emerging pollutants of severe environmental concern in water and wastewater: A comprehensive review on current developments and future research. *Water-Energy Nexus* **2023**, *6*, 74–95. [CrossRef]

2. Rhind, S.M. Anthropogenic pollutants: A threat to ecosystem sustainability? *Philos. Trans. R. Soc. Lond. B Biol. Sci.* **2009**, *364*, 3391–3401. [CrossRef] [PubMed]
3. Moussa, M.S.; Mostafa, M.K. Rapid Assessment Method for Evaluation of the Weighted Contribution of Anthropogenic Pollution: A Case Study of Lake Burullus, Egypt. *Water* **2021**, *13*, 3337. [CrossRef]
4. Egbueri, J.C.; Agbasi, J.C.; Ayejoto, D.A.; Khan, M.I.; Khan, M.Y.A. Extent of anthropogenic influence on groundwater quality and human health-related risks: An integrated assessment based on selected physicochemical characteristics. *Geocarto Int.* **2023**, *38*, 2210100. [CrossRef]
5. Busquets, R.; Ivanov, A.E.; Mbundi, L.; Hörberg, S.; Kozynchenko, O.P.; Cragg, P.J.; Savina, I.N.; Whitby, R.L.D.; Mikhalovsky, S.V.; Tennison, S.R.; et al. Carbon-cryogel hierarchical composites as effective and scalable filters for removal of trace organic pollutants from water. *J. Environ. Manag.* **2016**, *182*, 141–148. [CrossRef] [PubMed]
6. Ore, O.T.; Adeola, A.O.; Bayode, A.A.; Adedipe, D.T.; Nomngongo, P.N. Organophosphate pesticide residues in environmental and biological matrices: Occurrence, distribution and potential remedial approaches. *Environ. Chem. Ecotoxicol.* **2023**, *5*, 9–23. [CrossRef]
7. Banday, T.H.; Tathineni, B.; Desai, M.S.; Naik, V. Predictors of Morbidity and Mortality in Organophosphorus Poisoning: A Case Study in Rural Hospital in Karnataka, India. *N. Am. J. Med. Sci.* **2015**, *7*, 259–265. [CrossRef] [PubMed]
8. Aroniadou-Anderjaska, V.; Figueiredo, T.H.; de Araujo Furtado, M.; Pidoplichko, V.I.; Braga, M.F.M. Mechanisms of Organophosphate Toxicity and the Role of Acetylcholinesterase Inhibition. *Toxics* **2023**, *11*, 866. [CrossRef] [PubMed]
9. Alejo-González, K.; Hanson-Viana, E.; Vazquez-Duhalt, R. Enzymatic detoxification of organophosphorus pesticides and related toxicants. *J. Pestic. Sci.* **2018**, *43*, 1–9. [CrossRef]
10. Lu, Y.; Park, Y.; Gao, X.; Zhang, X.; Yao, J.; Pang, Y.-P.; Jiang, H.; Zhu, K.Y. Cholinergic and non-cholinergic functions of two acetylcholinesterase genes revealed by gene-silencing in Tribolium castaneum. *Sci. Rep.* **2012**, *2*, 288. [CrossRef]
11. Pope, C.; Karanth, S.; Liu, J. Pharmacology and toxicology of cholinesterase inhibitors: Uses and misuses of a common mechanism of action. *Environ. Toxicol. Pharmacol.* **2005**, *19*, 433–446. [CrossRef] [PubMed]
12. Chen, Z.-R.; Huang, J.-B.; Yang, S.-L.; Hong, F.-F. Role of Cholinergic Signaling in Alzheimer's Disease. *Molecules* **2022**, *27*, 1816. [CrossRef]
13. Facure, M.H.M.; Mercante, L.A.; Mattoso, L.H.C.; Correa, D.S. Detection of trace levels of organophosphate pesticides using an electronic tongue based on graphene hybrid nanocomposites. *Talanta* **2017**, *167*, 59–66. [CrossRef]
14. Nguyen, K.N.; Saxena, R.; Re, D.B.; Yan, B. Rapid LC-MS/MS quantification of Organophosphate non-specific metabolites in hair using alkaline extraction approach. *J. Chromatogr. B Analyt. Technol. Biomed. Life Sci.* **2023**, *1217*, 123619. [CrossRef] [PubMed]
15. Yang, Z.; Liu, Y.; Liu, D.; Zhou, Z. Determination of organophosphorus pesticides in soil by dispersive liquid-liquid microextraction and gas chromatography. *J. Chromatogr. Sci.* **2012**, *50*, 15–20. [CrossRef]
16. Kumaran, A.; Vashishth, R.; Singh, S.; Surendran, U.; James, A.; Chellam, P.V. Biosensors for detection of organophosphate pesticides: Current technologies and future directives. *Microchem. J.* **2022**, *178*, 107420. [CrossRef]
17. Karbelkar, A.A.; Reynolds, E.E.; Ahlmark, R.; Furst, A.L. A Microbial Electrochemical Technology to Detect and Degrade Organophosphate Pesticides. *ACS Cent. Sci.* **2021**, *7*, 1718–1727. [CrossRef]
18. Bhattu, M.; Verma, M.; Kathuria, D. Recent advancements in the detection of organophosphate pesticides: A review. *Anal. Methods* **2021**, *13*, 4390–4428. [CrossRef]
19. Shah, M.M.; Ren, W.; Irudayaraj, J.; Sajini, A.A.; Ali, M.I.; Ahmad, B. Colorimetric Detection of Organophosphate Pesticides Based on Acetylcholinesterase and Cysteamine Capped Gold Nanoparticles as Nanozyme. *Sensors* **2021**, *21*, 8050. [CrossRef] [PubMed]
20. Chaudhari, P.; Chau, L.-K.; Ngo, L.T.; Chang, T.-C.; Chen, Y.-L.; Huang, K.-T. Competitive Assay for the Ultrasensitive Detection of Organophosphate Pesticides Based on a Fiber-Optic Particle Plasmon Resonance Biosensor and an Acetylcholinesterase Binding Peptide. *Anal. Chem.* **2023**, *95*, 14600–14607. [CrossRef]
21. Bondžić, A.M.; Lazarević Pašti, T.D.; Pašti, I.A.; Bondžić, B.P.; Momčilović, M.D.; Loosen, A.; Parac-Vogt, T.N. Synergistic Effect of Sorption and Hydrolysis by NU-1000 Nanostructures for Removal and Detoxification of Chlorpyrifos. *ACS Appl. Nano Mater.* **2022**, *5*, 3312–3324. [CrossRef]
22. Karpouzas, D.G.; Singh, B.K. Microbial degradation of organophosphorus xenobiotics: Metabolic pathways and molecular basis. *Adv. Microb. Physiol.* **2006**, *51*, 119–185. [PubMed]
23. Kumar, S.; Kaushik, G.; Dar, M.A.; Nimesh, S.; LÓPez-Chuken, U.J.; Villarreal-Chiu, J.F. Microbial Degradation of Organophosphate Pesticides: A Review. *Pedosphere* **2018**, *28*, 190–208. [CrossRef]
24. Mali, H.; Shah, C.; Patel, D.H.; Trivedi, U.; Subramanian, R.B. Degradation insight of organophosphate pesticide chlorpyrifos through novel intermediate 2,6-dihydroxypyridine by Arthrobacter sp. HM01. *Bioresour. Bioprocess.* **2022**, *9*, 31. [CrossRef] [PubMed]
25. Mirković, M.M.; Pašti, T.D.L.; Došen, A.M.; Čebela, M.Ž.; Rosić, A.A.; Matović, B.Z.; Babić, B.M. Adsorption of malathion on mesoporous monetite obtained by mechanochemical treatment of brushite. *RSC Adv.* **2016**, *6*, 12219–12225. [CrossRef]
26. Alrefaee, S.H.; Aljohani, M.; Alkhamis, K.; Shaaban, F.; El-Desouky, M.G.; El-Bindary, A.A.; El-Bindary, M.A. Adsorption and effective removal of organophosphorus pesticides from aqueous solution via novel metal-organic framework: Adsorption isotherms, kinetics, and optimization via Box-Behnken design. *J. Mol. Liq.* **2023**, *384*, 122206. [CrossRef]

27. Fu, Q.; Jia, X.; Zhang, S.; Zhang, J.; Sun-Waterhouse, D.; Wang, C.; Waterhouse, G.I.N.; Wu, P. Highly defective copper-based metal-organic frameworks for the efficient adsorption and detection of organophosphorus pesticides: An experimental and computational investigation. *Food Chem.* **2023**, *423*, 136319. [CrossRef] [PubMed]
28. Sagar, V.; Kukkar, D. Facile adsorption of organophosphate pesticides over HKUST-1 MOFs. *Environ. Monit. Assess.* **2023**, *195*, 1056. [CrossRef] [PubMed]
29. Mahmoud, L.A.M.; Dos Reis, R.A.; Chen, X.; Ting, V.P.; Nayak, S. Metal-Organic Frameworks as Potential Agents for Extraction and Delivery of Pesticides and Agrochemicals. *ACS Omega* **2022**, *7*, 45910–45934. [CrossRef]
30. Bruna, F.; Pavlovic, I.; Barriga, C.; Cornejo, J.; Ulibarri, M.A. Adsorption of pesticides Carbetamide and Metamitron on organohydrotalcite. *Appl. Clay Sci.* **2006**, *33*, 116–124. [CrossRef]
31. Lazarević-Pašti, T.; Jocić, A.; Milanković, V.; Tasić, T.; Batalović, K.; Breitenbach, S.; Unterweger, C.; Fürst, C.; Pašti, I.A. Investigating the Adsorption Kinetics of Dimethoate, Malathion and Chlorpyrifos on Cellulose-Derived Activated Carbons: Understanding the Influence of Physicochemical Properties. *C J. Carbon Res.* **2023**, *9*, 103. [CrossRef]
32. Tasić, T.; Milanković, V.; Batalović, K.; Breitenbach, S.; Unterweger, C.; Fürst, C.; Pašti, I.A.; Lazarević-Pašti, T. Application of Viscose-Based Porous Carbon Fibers in Food Processing—Malathion and Chlorpyrifos Removal. *Foods* **2023**, *12*, 2362. [CrossRef] [PubMed]
33. El-Kady, A.A.; Abdel Ghafar, H.H.; Ibrahim, M.B.M.; Abdel-Wahhab, M.A. Utilization of activated carbon prepared from agricultural waste for the removal of organophosphorous pesticide from aqueous media. *Desalination Water Treat.* **2013**, *51*, 7276–7285. [CrossRef]
34. Tahmasebi, A.A.; Salimi Beni, A.; Azhdarpoor, A.; Moeini, Z. The application of granular and biological activated carbon columns in removal of organochlorine and organophosphorus pesticides in a water treatment plant. *J. Water Process Eng.* **2023**, *56*, 104383. [CrossRef]
35. Ioannidou, O.A.; Zabaniotou, A.A.; Stavropoulos, G.G.; Islam, M.A.; Albanis, T.A. Preparation of activated carbons from agricultural residues for pesticide adsorption. *Chemosphere* **2010**, *80*, 1328–1336. [CrossRef] [PubMed]
36. Jevremović, A.; Stanojković, A.; Arsenijević, D.; Arsenijević, A.; Arzumanyan, G.; Mamatkulov, K.; Petrović, J.; Nedić Vasiljević, B.; Bajuk-Bogdanović, D.; Milojević-Rakić, M. Mitigating toxicity of acetamiprid removal techniques–Fe modified zeolites in focus. *J. Hazard. Mater.* **2022**, *436*, 129226. [CrossRef] [PubMed]
37. Mostafa, M.; Bin Jumah, M.N.; Othman, S.I.; Alruhaimi, R.S.; Salama, Y.F.; Allam, A.A.; Abukhadra, M.R. Effective removal of different species of organophosphorus pesticides (acephate, omthosate, and methyl parathion) using chitosan/Zeolite-A as multifunctional adsorbent. *Environ. Technol. Innov.* **2021**, *24*, 101875. [CrossRef]
38. Bai, B.; Wu, N.; Yang, H.; Liu, H.; Jin, X.; Chen, L.; Huang, Z.; Zhou, C.; Wang, S.; Si, W. Development of a Zeolite H-ZSM-5-Based D-µSPE Method for the Determination of Organophosphorus Pesticides in Tea Beverages. *Processes* **2023**, *11*, 1027. [CrossRef]
39. Lazarević-Pašti, T.; Aníćijević, V.; Baljozović, M.; Aníćijević, D.V.; Gutić, S.; Vasić, V.; Skorodumova, N.V.; Pašti, I.A. The impact of the structure of graphene-based materials on the removal of organophosphorus pesticides from water. *Environ. Sci. Nano* **2018**, *5*, 1482–1494. [CrossRef]
40. Shi, X.; Cheng, C.; Peng, F.; Hou, W.; Lin, X.; Wang, X. Adsorption properties of graphene materials for pesticides: Structure effect. *J. Mol. Liq.* **2022**, *364*, 119967. [CrossRef]
41. Yadav, S.; Goel, N.; Kumar, V.; Singhal, S. Graphene Oxide as Proficient Adsorbent for the Removal of Harmful Pesticides: Comprehensive Experimental Cum DFT Investigations. *Anal. Chem. Lett.* **2019**, *9*, 291–310. [CrossRef]
42. Bruckmann, F.S.; Schnorr, C.; Oviedo, L.R.; Knani, S.; Silva, L.F.O.; Silva, W.L.; Dotto, G.L.; Bohn Rhoden, C.R. Adsorption and Photocatalytic Degradation of Pesticides into Nanocomposites: A Review. *Molecules* **2022**, *27*, 6261. [CrossRef] [PubMed]
43. Aníćijević, V.; Tasić, T.; Milanković, V.; Breitenbach, S.; Unterweger, C.; Fürst, C.; Bajuk-Bogdanović, D.; Pašti, I.A.; Lazarević-Pašti, T. How Well Do Our Adsorbents Actually Perform?-The Case of Dimethoate Removal Using Viscose Fiber-Derived Carbons. *Int. J. Environ. Res. Public Health* **2023**, *20*, 4553. [CrossRef] [PubMed]
44. Cordoba-Ramirez, M.; Chejne, F.; Alean, J.; Gómez, C.A.; Navarro-Gil, Á.; Ábrego, J.; Gea, G. Experimental strategy for the preparation of adsorbent materials from torrefied palm kernel shell oriented to CO_2 capture. *Environ. Sci. Pollut. Res.* **2024**, *31*, 18765–18784. [CrossRef] [PubMed]
45. Verner, A.; Tokarský, J.; Najser, T.; Matějová, L.; Kutláková, K.M.; Kielar, J.; Peer, V. Effects of Structure and Composition of Adsorbents on Competitive Adsorption of Gaseous Emissions: Experiment and Modeling. *Nanomaterials* **2023**, *13*, 724. [CrossRef] [PubMed]
46. Hadi, P.; Yeung, K.Y.; Barford, J.; An, K.J.; McKay, G. Significance of "effective" surface area of activated carbons on elucidating the adsorption mechanism of large dye molecules. *J. Environ. Chem. Eng.* **2015**, *3*, 1029–1037. [CrossRef]
47. Lawtae, P.; Tangsathitkulchai, C. The Use of High Surface Area Mesoporous-Activated Carbon from Longan Seed Biomass for Increasing Capacity and Kinetics of Methylene Blue Adsorption from Aqueous Solution. *Molecules* **2021**, *26*, 6521. [CrossRef]
48. Minović, T.Z.; Gulicovski, J.J.; Stoiljković, M.M.; Jokić, B.M.; Živković, L.S.; Matović, B.Z.; Babić, B.M. Surface characterization of mesoporous carbon cryogel and its application in arsenic (III) adsorption from aqueous solutions. *Microporous Mesoporous Mater.* **2015**, *201*, 271–276. [CrossRef]
49. Babić, B.; Kaluđerović, B.; Vračar, L.; Krstajić, N. Characterization of carbon cryogel synthesized by sol–gel polycondensation and freeze-drying. *Carbon* **2004**, *42*, 2617–2624. [CrossRef]

50. Babić, B.M.; Vračar, L.M.; Radmilović, V.; Krstajić, N.V. Carbon cryogel as support of platinum nano-sized electrocatalyst for the hydrogen oxidation reaction. *Electrochim. Acta* **2006**, *51*, 3820–3826. [CrossRef]
51. Momčilović, M.Z.; Ranđelović, M.S.; Onjia, A.; Zarubica, A.R.; Babić, B.M.; Matović, B. Study on the efficient removal of clopyralid from water using a resorcinol-formaldehyde carbon cryogel. *J. Serbian Chem. Soc.* **2014**, *79*, 481–494. [CrossRef]
52. Tonanon, N.; Tanthapanichakoon, W.; Yamamoto, T.; Nishihara, H.; Mukai, S.R.; Tamon, H. Influence of surfactants on porous properties of carbon cryogels prepared by sol–gel polycondensation of resorcinol and formaldehyde. *Carbon* **2003**, *41*, 2981–2990. [CrossRef]
53. Krstić, A.; Lolić, A.; Mirković, M.; Kovač, J.; Arsić, T.M.; Babić, B.; Kalijadis, A. Synthesis of nitrogen doped and nitrogen and sulfur co-doped carbon cryogels and their application for pharmaceuticals removal from water. *J. Environ. Chem. Eng.* **2022**, *10*, 108998. [CrossRef]
54. Sepehri, S.; García, B.B.; Zhang, Q.; Cao, G. Enhanced electrochemical and structural properties of carbon cryogels by surface chemistry alteration with boron and nitrogen. *Carbon* **2009**, *47*, 1436–1443. [CrossRef]
55. Zhou, Y.; Luo, L.; Yan, W.; Li, Z.; Fan, M.; Du, G.; Zhao, W. Controlled preparation of nitrogen-doped hierarchical carbon cryogels derived from Phenolic-Based resin and their CO_2 adsorption properties. *Energy* **2022**, *246*, 123367. [CrossRef]
56. Al-Hajri, W.; De Luna, Y.; Bensalah, N. Review on Recent Applications of Nitrogen-Doped Carbon Materials in CO_2 Capture and Energy Conversion and Storage. *Energy Technol.* **2022**, *10*, 2200498. [CrossRef]
57. Hou, Z.; Terakura, K. Effect of Nitrogen Doping on the Migration of the Carbon Adatom and Monovacancy in Graphene. *J. Phys. Chem. C* **2015**, *119*, 4922–4933. [CrossRef]
58. Inagaki, M.; Toyoda, M.; Soneda, Y.; Morishita, T. Nitrogen-doped carbon materials. *Carbon* **2018**, *132*, 104–140. [CrossRef]
59. Türkmen, D.; Bakhshpour, M.; Akgönüllü, S.; Aşır, S.; Denizli, A. Heavy Metal Ions Removal From Wastewater Using Cryogels: A Review. *Front. Sustain.* **2022**, *3*, 765592. [CrossRef]
60. Dinu, I.A.; Ghimici, L.; Raschip, I.E. Macroporous 3D Chitosan Cryogels for Fastac 10EC Pesticide Adsorption and Antibacterial Applications. *Polymers* **2022**, *14*, 3145. [CrossRef]
61. Badran, A.M.; Utra, U.; Yussof, N.S.; Bashir, M.J.K. Advancements in Adsorption Techniques for Sustainable Water Purification: A Focus on Lead Removal. *Separations* **2023**, *10*, 565. [CrossRef]
62. Sadegh, H.; Ali, G.A.M. Potential Applications of Nanomaterials in Wastewater Treatment: Nanoadsorbents Performance. In *Advanced Treatment Techniques for Industrial Wastewater*; Hussain, A., Ahmed, S., Eds.; IGI Global: Hershey, PA, USA, 2019; pp. 51–61.
63. Barrett, E.P.; Joyner, L.G.; Halenda, P.P. The Determination of Pore Volume and Area Distributions in Porous Substances. I. Computations from Nitrogen Isotherms. *J. Am. Chem. Soc.* **1951**, *73*, 373–380. [CrossRef]
64. Ellman, G.L.; Courtney, K.D.; Andres, V., Jr.; Feather-Stone, R.M. A new and rapid colorimetric determination of acetylcholinesterase activity. *Biochem. Pharmacol.* **1961**, *7*, 88–95. [CrossRef] [PubMed]
65. Al Othman, Z.A. A Review: Fundamental Aspects of Silicate Mesoporous Materials. *Materials* **2012**, *5*, 2874–2902. [CrossRef]
66. Monson, P.A. Understanding adsorption/desorption hysteresis for fluids in mesoporous materials using simple molecular models and classical density functional theory. *Microporous Mesoporous Mater.* **2012**, *160*, 47–66. [CrossRef]
67. Zhang, D.; Luo, R. Modifying the BET model for accurately determining specific surface area and surface energy components of aggregates. *Constr. Build. Mater.* **2018**, *175*, 653–663. [CrossRef]
68. Xia, X.-H.; Zhang, X.-F.; Yi, S.-Q.; Liu, H.-B.; Chen, Y.-X.; Chen, H.; Yang, L.; He, Y.-D. Preparation of high specific surface area composite carbon cryogels from self-assembly of graphene oxide and resorcinol monomers for supercapacitors. *J. Solid State Electrochem.* **2016**, *20*, 1793–1802. [CrossRef]
69. Job, N.; Théry, A.; Pirard, R.; Marien, J.; Kocon, L.; Rouzaud, J.-N.; Béguin, F.; Pirard, J.-P. Carbon aerogels, cryogels and xerogels: Influence of the drying method on the textural properties of porous carbon materials. *Carbon* **2005**, *43*, 2481–2494. [CrossRef]
70. White, R.J.; Budarin, V.; Luque, R.; Clark, J.H.; Macquarrie, D.J. Tuneable porous carbonaceous materials from renewable resources. *Chem. Soc. Rev.* **2009**, *38*, 3401–3418. [CrossRef]
71. Li, J.; Chen, X.; Gong, J.; Zhu, J.; Mijowska, E. Deep insight into the pore size distribution of N-doped porous carbon materials on electrochemical energy storage and CO_2 sorption. *Diam. Relat. Mater.* **2020**, *105*, 107802. [CrossRef]
72. Sun, A.; Liu, Y.; Ma, J.; Yang, L.; Wang, Y. Preparation and oxygen reduction performance of nitrogen-doped cotton stalk-derived carbon. *Int. J. Low-Carbon Technol.* **2022**, *17*, 1029–1035. [CrossRef]
73. Zheng, L.; Wang, X.; Wang, H.; Zhao, X.; Kong, F.; Liu, Y. Novel Nitrogen-Doped Porous Carbon with High Surface Areas Prepared from Industrial Alkali Lignin for Supercapacitors. *ChemElectroChem* **2022**, *9*, e202200869. [CrossRef]
74. Ferrari, A.C. Raman spectroscopy of graphene and graphite: Disorder, electron–phonon coupling, doping and nonadiabatic effects. *Solid State Commun.* **2007**, *143*, 47–57. [CrossRef]
75. Orlando, A.; Franceschini, F.; Muscas, C.; Pidkova, S.; Bartoli, M.; Rovere, M.; Tagliaferro, A. A Comprehensive Review on Raman Spectroscopy Applications. *Chemosensors* **2021**, *9*, 262. [CrossRef]
76. Ahmed, S.; Rafat, M.; Ahmed, A. Nitrogen doped activated carbon derived from orange peel for supercapacitor application. *Adv. Nat. Sci. Nanosci. Nanotechnol.* **2018**, *9*, 035008. [CrossRef]
77. Ferrari, A.C.; Robertson, J.; Ferrari, A.C.; Robertson, J. Raman spectroscopy of amorphous, nanostructured, diamond–like carbon, and nanodiamond. *Philos. Trans. R. Soc. London. Ser. A Math. Phys. Eng. Sci.* **2004**, *362*, 2477–2512. [CrossRef] [PubMed]

78. Brzhezinskaya, M.; Mishakov, I.V.; Bauman, Y.I.; Shubin, Y.V.; Maksimova, T.A.; Stoyanovskii, V.O.; Gerasimov, E.Y.; Vedyagin, A.A. One-pot functionalization of catalytically derived carbon nanostructures with heteroatoms for toxic-free environment. *Appl. Surf. Sci.* **2022**, *590*, 153055. [CrossRef]
79. Ma, C.; Min, J.; Gong, J.; Liu, X.; Mu, X.; Chen, X.; Tang, T. Transforming polystyrene waste into 3D hierarchically porous carbon for high-performance supercapacitors. *Chemosphere* **2020**, *253*, 126755. [CrossRef]
80. Rella, S.; Giuri, A.; Corcione, C.E.; Acocella, M.R.; Colella, S.; Guerra, G.; Listorti, A.; Rizzo, A.; Malitesta, C. X-ray photoelectron spectroscopy of reduced graphene oxide prepared by a novel green method. *Vacuum* **2015**, *119*, 159–162. [CrossRef]
81. Mitra, A.; Howli, P.; Sen, D.; Das, B.; Chattopadhyay, K.K. Cu_2O/g-C_3N_4 nanocomposites: An insight into the band structure tuning and catalytic efficiencies. *Nanoscale* **2016**, *8*, 19099–19109. [CrossRef]
82. Barth, G.; Linder, R.; Bryson, C. Advances in charge neutralization for XPS measurements of nonconducting materials. *Surf. Interface Anal.* **1988**, *11*, 307–311. [CrossRef]
83. Gengenbach, T.R.; Major, G.H.; Linford, M.R.; Easton, C.D. Practical guides for x-ray photoelectron spectroscopy (XPS): Interpreting the carbon 1s spectrum. *J. Vac. Sci. Technol. A* **2021**, *39*, 013204. [CrossRef]
84. Hulicova-Jurcakova, D.; Seredych, M.; Lu, G.Q.; Bandosz, T.J. Combined Effect of Nitrogen- and Oxygen-Containing Functional Groups of Microporous Activated Carbon on its Electrochemical Performance in Supercapacitors. *Adv. Funct. Mater.* **2009**, *19*, 438–447. [CrossRef]
85. Sobaszek, M.; Brzhezinskaya, M.; Olejnik, A.; Mortet, V.; Alam, M.; Sawczak, M.; Ficek, M.; Gazda, M.; Weiss, Z.; Bogdanowicz, R. Highly Occupied Surface States at Deuterium-Grown Boron-Doped Diamond Interfaces for Efficient Photoelectrochemistry. *Small* **2023**, *19*, 2208265. [CrossRef] [PubMed]
86. Gomez-Bolivar, J.; Mikheenko, I.P.; Orozco, R.L.; Sharma, S.; Banerjee, D.; Walker, M.; Hand, R.A.; Merroun, M.L.; Macaskie, L.E. Synthesis of Pd/Ru Bimetallic Nanoparticles by Escherichia coli and Potential as a Catalyst for Upgrading 5-Hydroxymethyl Furfural Into Liquid Fuel Precursors. *Front. Microbiol.* **2019**, *10*, 1276. [CrossRef] [PubMed]
87. Gutić, S.; Dobrota, A.S.; Gavrilov, N.; Baljozović, M.; Pašti, I.A.; Mentus, S.V. Surface Charge Storage Properties of Selected Graphene Samples in pH-neutral Aqueous Solutions of Alkali Metal Chlorides-Particularities and Universalities. *Int. J. Electrochem. Sci.* **2016**, *11*, 8662–8682. [CrossRef]
88. Sebastián, D.; Nieto-Monge, M.J.; Pérez-Rodríguez, S.; Pastor, E.; Lázaro, M.J. Nitrogen Doped Ordered Mesoporous Carbon as Support of PtRu Nanoparticles for Methanol Electro-Oxidation. *Energies* **2018**, *11*, 831. [CrossRef]
89. Kumar, S.S.; Ghosh, P.; Malyan, S.K.; Sharma, J.; Kumar, V. A comprehensive review on enzymatic degradation of the organophosphate pesticide malathion in the environment. *J. Environ. Sci. Health Part C* **2019**, *37*, 288–329. [CrossRef] [PubMed]
90. Wang, J.; Wang, J.; Zhu, L.; Xie, H.; Shao, B.; Hou, X. The enzyme toxicity and genotoxicity of chlorpyrifos and its toxic metabolite TCP to zebrafish Danio rerio. *Ecotoxicology* **2014**, *23*, 1858–1869. [CrossRef]
91. Aníćijević, V.J.; Petković, M.; Pašti, I.A.; Lazarević-Pašti, T.D. Decomposition of Dimethoate and Omethoate in Aqueous Solutions—Half-Life, Eco-Neurotoxicity Benchmarking, and Mechanism of Hydrolysis. *Water Air Soil Pollut.* **2022**, *233*, 390. [CrossRef]